CHAPTER 7

UPPER BOUND RIGID BLOCK METHOD FOR UNSATURATED SOIL SLOPES UNDER SEISMIC AND SURCHARGE LOADING CONDITIONS

7.1 INTRODUCTION AND REVIEW OF EXISTING STUDIES

The previous chapter demonstrates the stability analysis of homogeneous unsaturated soil slopes subjected to static loading condition by using the variational method. In the present chapter, the stability analysis of homogeneous unsaturated soil slopes under seismic and surcharge loading conditions is carried out by employing upper bound rigid block method (UBRBM). This method is based on the upper bound limit theorem (Drucker, 1951) wherein the chosen block mechanism is minimized for obtaining the upper bound collapse field and the corresponding stability. In the present chapter, the log-spiral failure mechanism is adopted for computing the slope stability. A good amount of research in the past (Oloo et al. 1997; Costa et al. 2003; Vanapalli and Mohamed 2007; Oh and Vanapalli 2011, 2013) proved that the physiochemical and capillary forces between the soil grains in the case of unsaturated soil, give rise to two additional stress parameters; namely, net normal stress and matric suction, which in turn increases the soil's shear strength. There are two-way approaches for analysing the strength behaviour within the vadose zone: a) matric suction based approach (Fredlund and Rahardjo 1993, Travis et al. 2010, Gavin and Xue 2010; Cho and Lee 2001, 2002, Cai and Ugai 2004, Hamdhan and Schweiger 2013; Sun et al. 2016; Kang et al. 2020), and b) suction-stress based approach (Griffiths and Lu 2005, Lu and Godt 2008, Griffiths and Lu 2005, Vahedifard et al. 2015a, Vahedifard et al. 2015b, Vahedifard et al. 2016, Sun et al. 2019, Thota and Vahedifard 2021). Owing to the advantages of suction-stress over the matric suction, the partially-saturated is modelled on the basis of suction-stress based effective stress equations. However, no literature seems to be available to assess the stability of unsaturated slopes subjected to surcharge and seismic loads. An effort has been exerted in this regard to evaluate the stability of homogeneous unsaturated soil slopes under surcharge and seismic loads by using UBRBM. The study is carried out for various flow conditions: hydrostatic, infiltration (negative), and evaporation (positive). The variation in depth of the water table is also incorporated. An extensive parametric analysis was performed, and stability charts were presented for various slope geometry combinations, soil strength properties, hydro-mechanical parameters, water table depth, flow conditions, surcharge, and seismic loads

7.2 PROBLEM STATEMENT AND MODEL FORMULATION

Fig. 7.1 depicts a representative homogeneous and isotropic, cohesive-frictional, unsaturated soil slope on which the effects of seismic forces and surcharge pressures are verified. Following traditional and contemporary practices (Choudhury and Ahmad 2007, Zhao et al. 2016) the seismic activity on the slope is idealized by the pseudo-static horizontal (F_h=k_hW) and vertical (F_v=k_vW) seismic forces; here, k_h and k_v represent horizontal and vertical seismic coefficients, respectively, and W represents the weight of the failed soil block, as illustrated in Fig. 7.1a. The form of the surcharge pressure, p_s, chosen for the problem is demonstrated in Fig. 7.1b. The geometry of the slope is represented by its (a) height H, (b) slope angle, β, and (c) ground surface inclination, ω. The water table is located at a depth of h_w from the toe of the slope. The fluid flow condition is assumed to be the same as the previous problem illustrated in Section 6.2. The variation of matric suction in the vadose soil zone is captured by using the van-Genuchten (1980) SWCC model. The permeability variation in the unsaturated zone is modeled by using Gardner's (1958) hydraulic conductivity function. The representative equations are given in Section 6.2.1.

Based on the upper bound limit analysis the soil is further assumed to be perfectly plastic, following linear Mohr-Coulomb yield envelope, and the associated flow rule. After the inclusion of the suction stress parameter, the modified Mohr yield envelope takes the form as given in Eqs. (6.9b), (6.9c).

This can be interpreted as the fact that the soil's overall shear strength at every point in the vadose zone enhances to some degree. Due to the variation in suction stress, the Mohr yield circle and Mohr yield envelope becomes spatially dependent along the vertical axis. Based on the upper bound rigid block method, the stability analysis of unsaturated soil slopes are performed by incorporating the suction stress characteristic curve (SSCC) along with the effects of pseudo-static forces and surcharge loads.

7.3 UPPER BOUND LIMIT ANALYSIS

7.3.1 Overview

The upper-bound theorem of limit analysis is a highly effective tool to encounter the stability problems in geotechnical engineering (Chen 1975; Sloan and Kleeman 1995; Soubra 1999; Zhu 2000; Kumar and Samui 2006; Kumar and Kouzer 2008; Kumar and Chakraborty 2014; Chakraborty and Kumar 2015; Chen and Xiao 2020). In the present study, the rigid-block based upper bound stability analysis is performed by a suitable assumption of the collapse mechanism. In the conventional finite element–based limit analysis methods, no such prior assumption of collapse mechanism is required; nevertheless, the present technique is adopted due to its easiness, simplicity, and computational flexibility. Based on this theorem, a suitable

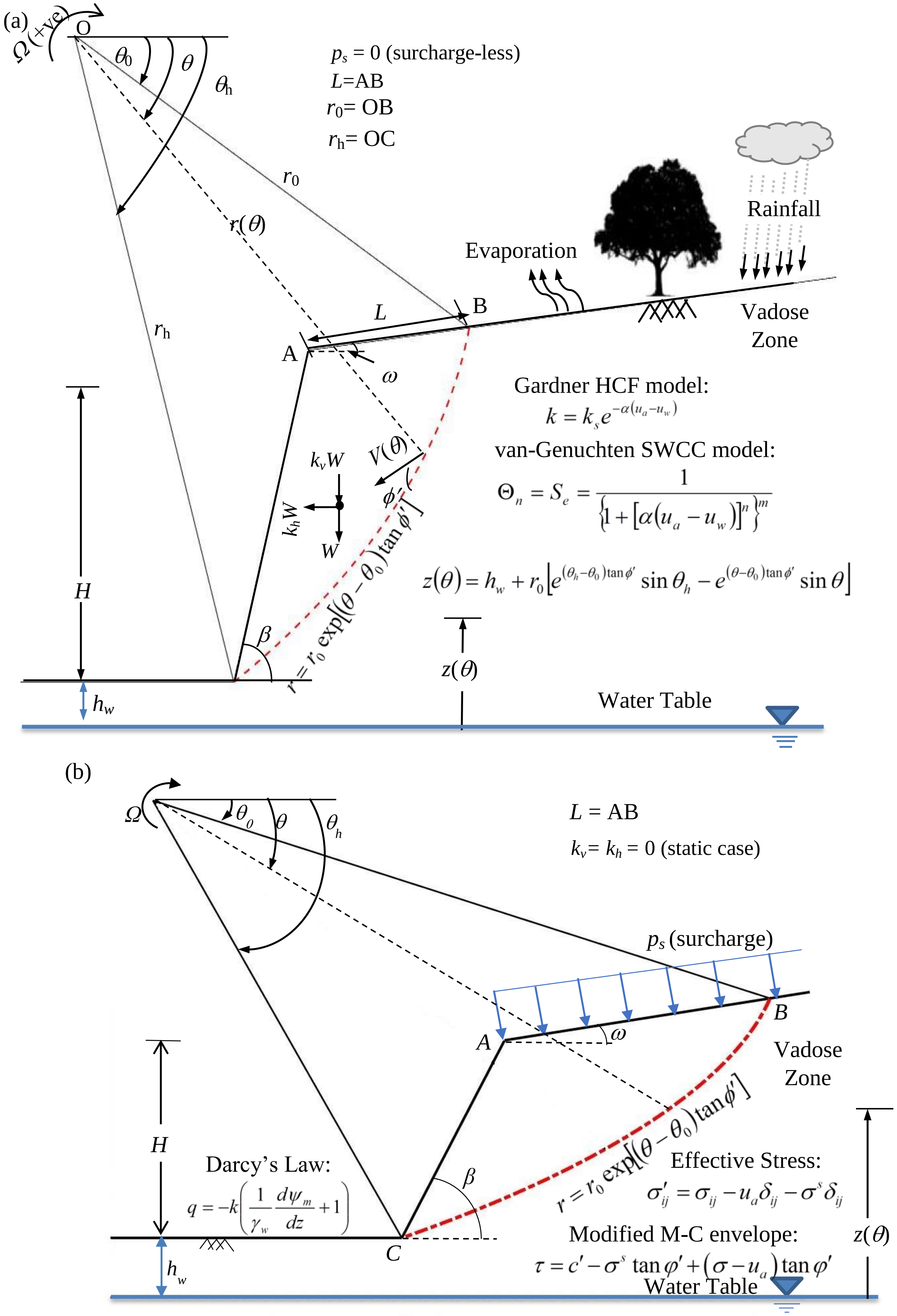

Fig. 7.1 Schematic representation of the chosen unsaturated soil slope of angle β subjected to: (a) seismic activity without surcharge, (b) surcharge load without any seismic forces.

collapse mechanism is chosen, and an upper-bound solution is derived from the work balance equation. To arrive at an upper-bound solution, the rigid blocks must be chosen in such a way so that the mechanism always remains kinematically admissible. The objective function is obtained by equating the rate of total external work $(\dot{W})$ with the total internal power dissipation ($\dot{D}$). This objective function is minimized to provide the upper-bound solutions, and the geometrical configuration of the failure mechanism. The yield surface is convex, and hence, the local minimizer is also a global minimizer.

7.3.2 Collapse mechanism and formulations

The log-spiral failure mechanism is regarded as one of the most appropriate failure mechanisms to model the soil slopes. A few literatures (Vahedifard et al. 2016, Sun et al. 2019) also suggested that the toe failure is the commonly seen failure-type for shallow slopes. Following the past studies, the shallow slope is assumed to fail by developing a log-spiral failure surface which passes through the toe and maintain the following equation: $r = r_0 e^{(\theta-\theta_0)\tan\phi'}$; here, r is any arbitrary radius vector and θ is the subtended angle (measured clock wise) between the horizontal axis and r vector. (r_0 , θ_0) and (r_h, θ_h) are the sets of first (OB) and last (OC) radius vectors and their corresponding subtended angles. Fig. 7.1 clearly describes the meaning of all the parameters for any arbitrary log-spiral mechanism having centre point at O. The log spiral meets the top ground surface of the slope at point B. The length of AB is denoted by L. By simple geometric relationship, the following two nondimensional length ratios are obtained (Chen 1975):

$$\frac{H}{r_0} = \frac{\sin\beta}{\sin(\beta-\omega)}\left\{\sin(\theta_h+\omega)e^{(\theta_h-\theta_0)\tan\phi'} - \sin(\theta_0+\omega)\right\} \tag{7.1}$$

$$\frac{L}{r_0} = \frac{\sin(\theta_h-\theta_0)}{\sin(\theta_h+\omega)} - \frac{\sin(\theta_h+\beta)}{\sin(\theta_h+\omega)\sin(\beta-\omega)}\left\{e^{(\theta_h-\theta_0)\tan\phi'} - \sin(\theta_h+\omega)\right\} \tag{7.2}$$

As per the upper bound theorem, $\dot{W} = \dot{D}$. The expression of these terms are evaluated as below.

7.3.2.1 Rate of external work done ($\dot{W}$)

In the presence of pseudo-static loading and the surcharge pressure, the total rate of external work done $\dot{W}$ constitutes the following:

(a) rate of work done by the weight of failed soil block ($\dot{W}_{weight}$),

(b) rate of work done by pseudo-static seismic forces ($\dot{W}_{earthquake}$), and

(c) rate of work done by surcharge loads ($\dot{W}_{surcharge}$).

The following section elaborates the development of each of the component.

7.3.2.1.1. Due to the gravitational forces ($\dot{W}_{weight}$)

Following the work of Chen (1975) and Utili (2014), the final form of the work done rate by the weight of the failed soil block is expressed as:

$$\dot{W}_{weight} = \gamma r_0^3 \Omega \left(f_1 - f_2 - f_3 \right) \tag{7.3}$$

$$f_1(\theta_h, \theta_0) = \frac{1}{3\left(1 + 9\tan^2\phi'\right)} \left\{ 3\tan\phi' \cos\theta_h + \sin\theta_h e^{3(\theta_h - \theta_0)\tan\phi'} - \left(3\tan\phi' \cos\theta_0 + \sin\theta_0\right) \right\} \tag{7.4}$$

$$f_2(\theta_h, \theta_0) = \frac{1}{6}\frac{L}{r_0}\left(2\cos\theta_0 - \frac{L}{r_0}\cos\omega\right)\sin(\theta_0 + \omega) \tag{7.5}$$

$$f_3(\theta_h, \theta_0) = \frac{1}{6} e^{(\theta_h - \theta_0)\tan\phi'} \left[\sin(\theta_h - \theta_0) - \frac{L}{r_0}\sin(\theta_h + \omega)\right]\left[\cos\theta_0 - \frac{L}{r_0}\cos\omega + \cos\theta_h e^{(\theta_h - \theta_0)\tan\phi'}\right] \tag{7.6}$$

Here, *Ω* is the rate of the angular velocity of sliding mass (clockwise considered positive), and *L/r₀* is a function of *θ₀* and *θ_h,* as mentioned in Eq. (7.2).

7.3.2.1.2. Due to the application of seismic forces ($\dot{W}_{earthquake}$):

To simplify the complexities involved in the dynamic analysis, of earthquake forces, the pseudo-static analysis is engrained into the formulations by factoring in the seismic acceleration coefficients. In the present analysis procedure, the vertical seismic force is assumed to play in the vertical downward direction. The expressions of work done by the pseudo-static forces have been given by Zhao (2016) and are presented below:

$$\dot{W}_{earthquake} = \gamma r_0^3 \Omega k_v \left(f_1 - f_2 - f_3\right) + \gamma r_0^3 \Omega k_h \left(f_4 - f_5 - f_6\right) \tag{7.7}$$

$$f_4\left(\theta_h, \theta_0\right) = \frac{e^{3\tan\phi'(\theta_h - \theta_0)}\left(3\tan\phi' \sin\theta_h - \cos\theta_h\right) - 3\tan\phi' \sin\theta_0 + \cos\theta_0}{3\left(1 + 9\tan^2\phi'\right)} \tag{7.8}$$

$$f_5\left(\theta_h, \theta_0\right) = \frac{1}{6}\frac{L}{r_0}\left(2\sin\theta_0 + \frac{L}{r_0}\sin\omega\right)\sin\left(\theta_0 + \omega\right) \tag{7.9}$$

$$f_6\left(\theta_h, \theta_0\right) = \frac{1}{6} e^{(\theta_h - \theta_0)\tan\phi'}\left[\sin\left(\theta_h - \theta_0\right) - \frac{L}{r_0}\sin\left(\theta_h + \omega\right)\right]\left[\sin\theta_0 + \frac{L}{r_0}\sin\omega + \sin\theta_h e^{(\theta_h - \theta_0)\tan\phi'}\right] \tag{7.10}$$

It can be noted that unlike the $\dot{W}_{weight}$ term, the $\dot{W}_{earthquake}$ term involves the effect of the vertical as well as horizontal forces; nevertheless, the basic architecture of $\dot{W}_{weight}$ and $\dot{W}_{earthquake}$ remain the same.

7.3.2.1.3. Due to the application of surcharge pressure ($\dot{W}_{surch\arg e}$):

By simple trigonometric relationship, the rate of work done by the uniformly distributed surcharge load can be expressed as follows:

$$\dot{W}_{surchage} = \left(p_s L\right)\Omega\left(r_0 \cos\theta_0 - 0.5L\cos\omega\right) \tag{7.11a}$$

$$\Rightarrow \dot{W}_{surchage} = p_s \Omega r_0^2 \left(\frac{L}{r_0}\cos\theta_0 - 0.5\frac{L^2}{r_0^2}\cos\omega\right) \tag{7.11b}$$

7.3.2.2 Rate of energy dissipation

Due to the rotational sliding mechanism, the energy dissipated ($\dot{D}$) across the log spiral surface, CB, can be expressed as:

$$\dot{D} = \int_{\theta_0}^{\theta_h} c'_{total}\left(V\cos\phi'\right)\frac{rd\theta}{\cos\phi'} \tag{7.12}$$

where, $c'_{total} = c' + c'_{apparent}$. Plugging the values of c' and $c'_{apparent}$ the expression of $\dot{D}$ can be decoupled as following:

$$\dot{D} = \int_{\theta_0}^{\theta_h} \left(c' + c'_{apparent}\right)\left(V\cos\phi'\right)\frac{rd\theta}{\cos\phi'} \tag{7.13}$$

$$\dot{D} = \dot{D}_{cohesion} + \dot{D}_{suction} = \underbrace{\int_{\theta_0}^{\theta_h} c'\left(V\cos\phi'\right)\frac{rd\theta}{\cos\phi'}}_{\substack{\text{Dissipation} \\ \text{component due to} \\ \text{internal cohesion} \\ (\dot{D}_{cohesion})}} + \underbrace{\int_{\theta_0}^{\theta_h} c'_{apparent}\left(V\cos\phi'\right)\frac{rd\theta}{\cos\phi'}}_{\substack{\text{Dissipation} \\ \text{component due to} \\ \text{suction stress} \\ (\dot{D}_{suction})}} \tag{7.14}$$

The contributions to energy dissipations by the soil's internal cohesion and by the matric suction are separately analyzed below:

7.3.2.2.1 Due to the internal cohesion ($\dot{D}_{cohesion}$):

$$\dot{D}_{cohesion} = \int_{\theta_0}^{\theta_h} c'\left(V\cos\phi'\right)\frac{rd\theta}{\cos\phi'} = \int_{\theta_0}^{\theta_h} c'\left(r\Omega\right)rd\theta$$

(From Eq. (7.14) and using *V=rΩ*)

$$= \int_{\theta_0}^{\theta_h} c'\Omega\, r^2 d\theta \tag{7.15a}$$

$$\dot{D}_{cohesion} = \int_{\theta_0}^{\theta_h} c'\Omega\, r_0^2 e^{2(\theta-\theta_0)\tan\phi'} d\theta = \frac{c' r_0^2 \Omega}{2\tan\phi'}\left[e^{2(\theta_h-\theta_0)\tan\phi'} - 1\right] \tag{7.15b}$$

7.3.2.2.2 Due to the suction ($\dot{D}_{suction}$):

$$\dot{D}_{suction} = \int_{\theta_0}^{\theta_h} c'_{apparent}\left(V\cos\phi'\right)\frac{rd\theta}{\cos\phi'} \tag{7.16}$$

Combining the expressions of $c'_{apparent}$ ($c'_{apparent} = -\sigma^s\tan\phi'$), σ^s (Eq. 6.11), and Eq. 7.16, the following relation is obtained.

$$\dot{D}_{suction} = \int_{\theta_0}^{\theta_h} \left(-\sigma^s\tan\phi'\right)\left(V\cos\phi'\right)\frac{rd\theta}{\cos\phi'}$$

$$\dot{D}_{suction} = \int_{\theta_0}^{\theta_h} -\frac{1}{\alpha}\frac{\ln\left[\left(1+\frac{q}{k_s}\right)\mathrm{e}^{-\alpha\gamma_w z}-\frac{q}{k_s}\right]}{\left(1+\left\{-\ln\left[\left(1+\frac{q}{k_s}\right)\mathrm{e}^{-\alpha\gamma_w z}-\frac{q}{k_s}\right]\right\}^n\right)^{1-1/n}}\tan\phi'\Omega r^2 d\theta$$

$$\Rightarrow \dot{D}_{suction} = \int_{\theta_0}^{\theta_h} -\frac{1}{\alpha}\frac{\ln\left[\left(1+\frac{q}{k_s}\right)\mathrm{e}^{-\alpha\gamma_w z}-\frac{q}{k_s}\right]}{\left(1+\left\{-\ln\left[\left(1+\frac{q}{k_s}\right)\mathrm{e}^{-\alpha\gamma_w z}-\frac{q}{k_s}\right]\right\}^n\right)^{1-1/n}}\tan\phi'\Omega r_0^2 e^{(\theta-\theta_0)\tan\phi'} d\theta \tag{7.17}$$

here, z (positive upwards) represents an arbitrary distance above the GWT in the vadose zone. The relationship between z and θ can be further expressed as:

$$z(\theta) = h_w + r_0\left[e^{(\theta_h-\theta_0)\tan\phi'}\sin\theta_h - e^{(\theta-\theta_0)\tan\phi'}\sin\theta\right] \tag{7.18}$$

Upon substituting the expression of $z(\theta)$ in Eq. (7.17) the term $\dot{D}_{suction}$ becomes an integral in terms of θ. Due to the immense complexities involved in finding the closed-form integral solution, the above integration was solved numerically by using Gauss Quadrature scheme in *MATLAB*.

Therefore, the total rate of energy dissipation conforms to the following equation:

$$\dot{D}=\frac{c' r_0^2\Omega}{2\tan\phi'}\left[e^{2(\theta_h-\theta_0)\tan\phi'}-1\right]+\int_{\theta_0}^{\theta_h}-\frac{1}{\alpha}\frac{\ln\left[\left(1+\frac{q}{k_s}\right)e^{-\alpha\gamma_w z(\theta)}-\frac{q}{k_s}\right]\tan\phi'\Omega r_0^2 e^{(\theta-\theta_0)\tan\phi'}}{\left(1+\left\{-\ln\left[\left(1+\frac{q}{k_s}\right)e^{-\alpha\gamma_w z(\theta)}-\frac{q}{k_s}\right]\right\}^{n}\right)^{1-1/n}}d\theta \tag{7.19}$$

7.3.2.3 Determining the stability number by equating $\dot{W}=\dot{D}$

Applying the theorem of upper bound limit analysis, the rate of external work done by external forces is equated with the internal power dissipation and thereafter, the stability number is obtained as below:

7.3.2.3.1 For pseudo-static forces (without surcharge loads)

$$\gamma r_0^3\Omega(1+k_v)(f_1-f_2-f_3)+\gamma r_0^3\Omega k_h(f_4-f_5-f_6)=$$

$$\frac{c' r_0^2\Omega}{2\tan\phi'}\left[e^{2(\theta_h-\theta_0)\tan\phi'}-1\right]+\int_{\theta_0}^{\theta_h}-\frac{1}{\alpha}\frac{\ln\left[\left(1+\frac{q}{k_s}\right)\mathrm{e}^{-\alpha\gamma_w z}-\frac{q}{k_s}\right]}{\left(1+\left\{-\ln\left[\left(1+\frac{q}{k_s}\right)\mathrm{e}^{-\alpha\gamma_w z}-\frac{q}{k_s}\right]\right\}^{n}\right)^{1-1/n}}\tan\phi'\Omega r_0^2 e^{(\theta-\theta_0)\tan\phi'}d\theta$$

$$\Rightarrow \gamma r_0\left[(1+k_v)(f_1-f_2-f_3)+k_h(f_4-f_5-f_6)\right]=$$

$$\frac{c'}{2\tan\phi'}\left[e^{2(\theta_h-\theta_0)\tan\phi'}-1\right]+\int_{\theta_0}^{\theta_h}-\frac{1}{\alpha}\frac{\ln\left[\left(1+\frac{q}{k_s}\right)\mathrm{e}^{-\alpha\gamma_w z}-\frac{q}{k_s}\right]}{\left(1+\left\{-\ln\left[\left(1+\frac{q}{k_s}\right)\mathrm{e}^{-\alpha\gamma_w z}-\frac{q}{k_s}\right]\right\}^{n}\right)^{1-1/n}}\tan\phi' e^{(\theta-\theta_0)\tan\phi'}d\theta \tag{7.20}$$

Putting the value of H/r_0 from Eq. (7.1) into Eq. (7.20),

$$\Rightarrow \gamma H\left[\frac{\sin(\beta-\omega)}{\sin\beta\left\{\sin(\theta_h+\omega)e^{(\theta_h-\theta_0)\tan\phi'}-\sin(\theta_0+\omega)\right\}}\right]\left[(1+k_v)(f_1-f_2-f_3)+k_h(f_4-f_5-f_6)\right]=$$

$$\frac{c'}{2\tan\phi'}\left[e^{2(\theta_h-\theta_0)\tan\phi'}-1\right]+\int_{\theta_0}^{\theta_h}-\frac{1}{\alpha}\frac{\ln\left[\left(1+\frac{q}{k_s}\right)\mathrm{e}^{-\alpha\gamma_w z}-\frac{q}{k_s}\right]}{\left(1+\left\{-\ln\left[\left(1+\frac{q}{k_s}\right)\mathrm{e}^{-\alpha\gamma_w z}-\frac{q}{k_s}\right]\right\}^{n}\right)^{1-1/n}}\tan\phi' e^{(\theta-\theta_0)\tan\phi'}d\theta$$

$$\Rightarrow \frac{\gamma H}{c'} = \left(\frac{ \frac{1}{2\tan\phi'}\left[e^{2(\theta_h-\theta_0)\tan\phi'}-1\right] + \int_{\theta_0}^{\theta_h} -\frac{1}{c'\alpha} \frac{\ln\left[\left(1+\frac{q}{k_s}\right)\mathrm{e}^{-\alpha\gamma_w z}-\frac{q}{k_s}\right]}{\left(1+\left\{-\ln\left[\left(1+\frac{q}{k_s}\right)\mathrm{e}^{-\alpha\gamma_w z}-\frac{q}{k_s}\right]\right\}^{n}\right)^{1-1/n}} \tan\phi' e^{(\theta-\theta_0)\tan\phi'}\,d\theta }{ \left[\frac{\sin(\beta-\omega)}{\sin\beta\left\{\sin(\theta_h+\omega)e^{(\theta_h-\theta_0)\tan\phi'}-\sin(\theta_0+\omega)\right\}}\right] \left[(1+k_v)(f_1-f_2-f_3)+k_h(f_4-f_5-f_6)\right]} \right) \tag{7.21}$$

7.3.2.3.2 For surcharge loads (without pseudo-static forces)

$$\gamma r_0^3\Omega(f_1-f_2-f_3)+p_s\Omega r_0^2\left(\frac{L}{r_0}\cos\theta-0.5\frac{L^2}{r_0^2}\cos\omega\right)=$$

$$\frac{c' r_0^2\Omega}{2\tan\phi'}\left[e^{2(\theta_h-\theta_0)\tan\phi'}-1\right]+\int_{\theta_0}^{\theta_h}-\frac{1}{\alpha}\frac{\ln\left[\left(1+\frac{q}{k_s}\right)\mathrm{e}^{-\alpha\gamma_w z}-\frac{q}{k_s}\right]}{\left(1+\left\{-\ln\left[\left(1+\frac{q}{k_s}\right)\mathrm{e}^{-\alpha\gamma_w z}-\frac{q}{k_s}\right]\right\}^{n}\right)^{1-1/n}}\tan\phi'\Omega r_0^2 e^{(\theta-\theta_0)\tan\phi'}\,d\theta \tag{7.22}$$

$$\Rightarrow \gamma r_0(f_1-f_2-f_3)+p_s\left(\frac{L}{r_0}\cos\theta-0.5\frac{L^2}{r_0^2}\cos\omega\right)=$$

$$\frac{c'}{2\tan\phi'}\left[e^{2(\theta_h-\theta_0)\tan\phi'}-1\right]+\int_{\theta_0}^{\theta_h}-\frac{1}{\alpha}\frac{\ln\left[\left(1+\frac{q}{k_s}\right)\mathrm{e}^{-\alpha\gamma_w z}-\frac{q}{k_s}\right]}{\left(1+\left\{-\ln\left[\left(1+\frac{q}{k_s}\right)\mathrm{e}^{-\alpha\gamma_w z}-\frac{q}{k_s}\right]\right\}^{n}\right)^{1-1/n}}\tan\phi' e^{(\theta-\theta_0)\tan\phi'}\,d\theta$$

Substituting the value of H/r_0 from Eq. (7.1) into Eq. (7.22),

$$\Rightarrow \gamma H\left[\frac{\sin(\beta-\omega)}{\sin\beta\left\{\sin(\theta_h+\omega)e^{(\theta_h-\theta_0)\tan\phi'}-\sin(\theta_0+\omega)\right\}}\right](f_1-f_2-f_3)+p_s\left(\frac{L}{r_0}\cos\theta-0.5\frac{L^2}{r_0^2}\cos\omega\right)=$$

$$\frac{c'}{2\tan\phi'}\left[e^{2(\theta_h-\theta_0)\tan\phi'}-1\right]+\int_{\theta_0}^{\theta_h}-\frac{1}{\alpha}\frac{\ln\left[\left(1+\frac{q}{k_s}\right)\mathrm{e}^{-\alpha\gamma_w z}-\frac{q}{k_s}\right]}{\left(1+\left\{-\ln\left[\left(1+\frac{q}{k_s}\right)\mathrm{e}^{-\alpha\gamma_w z}-\frac{q}{k_s}\right]\right\}^{n}\right)^{1-1/n}}\tan\phi' e^{(\theta-\theta_0)\tan\phi'}\,d\theta$$

$$\Rightarrow \frac{\gamma H}{c'} = \left(\frac{A - \frac{p_s}{c'}\left(\frac{L}{r_0}\cos\theta - 0.5\frac{L^2}{r_0^2}\cos\omega \right) + \frac{1}{2\tan\phi'}\left[e^{2(\theta_h-\theta_0)\tan\phi'} - 1 \right]}{\left[\frac{\sin(\beta-\omega)}{\sin\beta\left\{ \sin(\theta_h+\omega)e^{(\theta_h-\theta_0)\tan\phi'} - \sin(\theta_0+\omega) \right\}} \right]\left(f_1 - f_2 - f_3 \right)} \right) \qquad (7.23)$$

where, $A = \int_{\theta_0}^{\theta_h} -\frac{1}{c'\alpha} \frac{\ln\left[\left(1+\frac{q}{k_s} \right) \mathrm{e}^{-\alpha\gamma_{\mathrm{w}} z} - \frac{q}{k_s} \right] \tan\phi' e^{(\theta-\theta_0)\tan\phi'}}{\left(1 + \left\{ -\ln\left[\left(1+\frac{q}{k_s} \right) \mathrm{e}^{-\alpha\gamma_{\mathrm{w}} z} - \frac{q}{k_s} \right] \right\}^n \right)^{1-1/n}} d\theta$

7.3.3 Stability number and numerical tool

The stability number characterizes the overall stability of the aforementioned slope, defined as $S_n=\gamma H/c'$ (Chen 1975), where H represents the maximum height the slope can retain, corresponding to a factor of safety equal to unity. As Eqs. (7.21) and (7.23) are highly non-linear, hence the term $\gamma H/c'$ itself becomes an irreducible and fundamental function of H, θ_0, θ_h ; but, the geometric parameters defining the mechanisms are only θ_0 and θ_h. Therefore, an implicit method is used to carry out the optimization, wherein instead of optimizing the term $\gamma H/c'$, the unit weight γ, which is function of H, c', θ_0, and θ_h is used as an objective function. For each computation, arbitrary values of H and c' are selected and plugged into Eqs. (7.21) and (7.23). The unit weight γ is minimized with respect to parameters r_0 and r_h, subject to the following constraints:

(i) $\theta_0 \leq \theta_h$; (ii) $\theta_0 \geq 0$; (iii) $\theta_h \geq 0$; (iv) $L/r_0 \geq 0$; and (v) $H/r_0 \geq 0$.

Suitable codes are written in *MATLAB 2018a*, and the optimization process is carried out using the FMINCON function on an Intel(R) Core(TM) i5-7200U CPU.

Finally, stability numbers are reported as $S_n=\gamma H/c'$ by plugging back the arbitrarily chosen values of H and c'.

7.4 PARAMETRIC STUDY

This section investigates the stability of unsaturated slopes subjected to pseudo-static forces and surcharge pressures by conducting an extensive parametric analysis. A detailed analysis is carried out to understand how the stability number (S_n) gets influenced by the effect of soil types (characterized by soil strength and vG parameters), seismic conditions (k_h and $\lambda= k_v/k_h$), GWT depth (h_w), flow conditions (Q), and surcharge loadings (p_s). The obtained results are elaborately discussed, in turn.

7.4.1 Impact of β and ϕ' on S_n

Figs. 7.2 and 7.3 present the variation of S_n with slope angles (β) and effective friction angle (ϕ') corresponding to k_h=0.1, and k_h=0.3, respectively. The S_n versus β and S_n versus ϕ' are designated here as $S_n(\beta)$ and $S_n(\phi')$ curves and they are represented with solid and dashed lines, respectively. The range of β (40°–90°) and ϕ' (15°–40°) are chosen in a large scale. The analyses in this section were carried out for (a) two different λ's (λ=0 and λ=1), (b) three different AEVs (α=0.1, 0.01 and 0.001 kPa^{-1}), and (c) different flow conditions (namely, evaporation (EV), infiltration (IF), no-flow (NF), and no-suction (NS)). The flow ratio chosen for EV and IF are 0.5 and –0.5, respectively. The NS curves, in a sense, represents the stability of the completely saturated soils. The desaturation rate is taken to be the same (n=3.0) for all the cases. While plotting $S_n(\beta)$, ϕ' is taken as 30°, and for examining $S_n(\phi')$ curves, β is considered to be 45°. Evidently, S_n decreases with the (a) increase in β, and (b) decrease in ϕ'. The stability value reduces significantly for k_h=0.3. However, the variation of λ does not

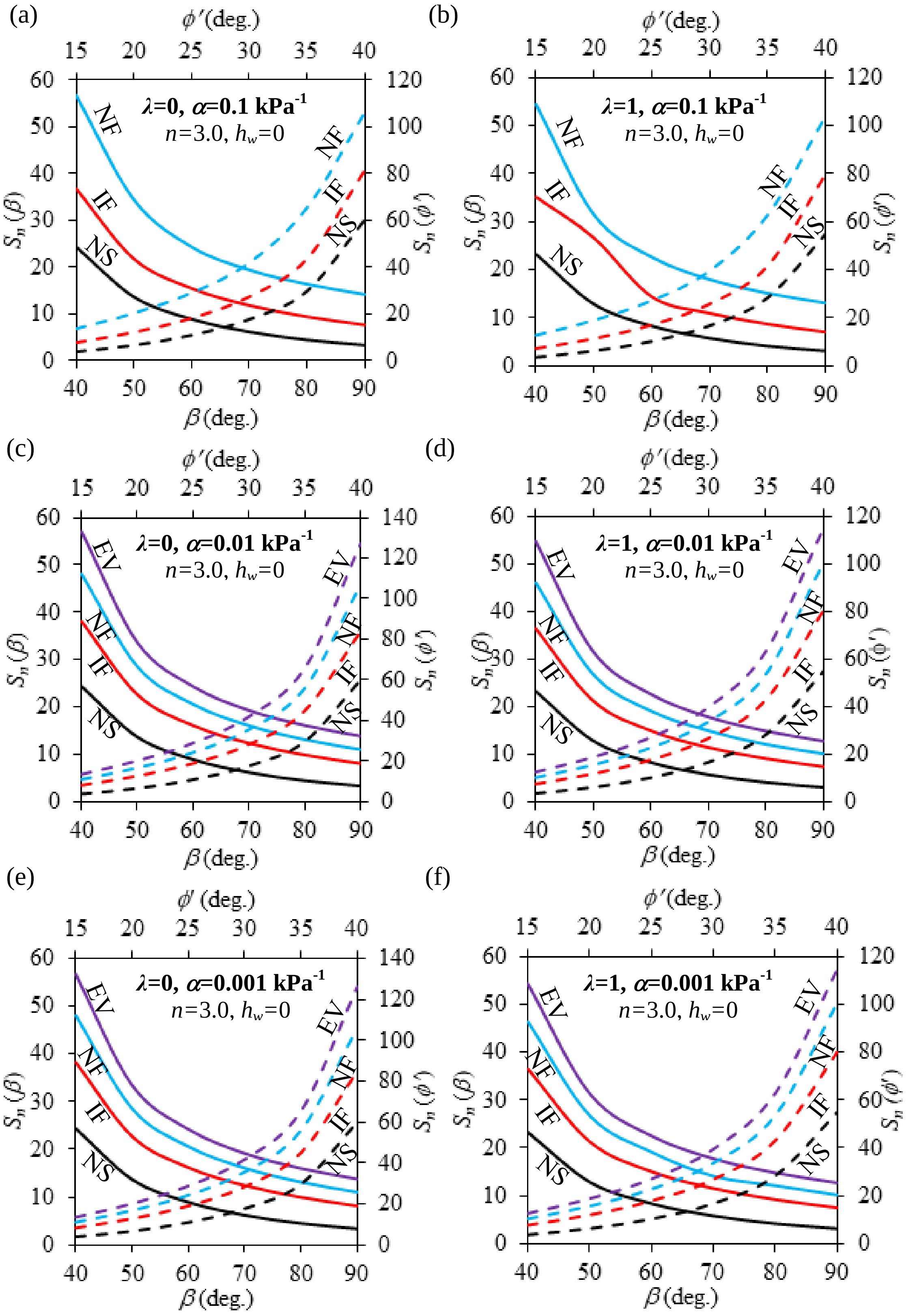

Note: (i) Solid and dashed lines represent S_n (β) and S_n (ϕ'), respectively.
(ii) EV: Evaporation; NF: No-Flow; IF: Infiltration; NS: No Suction

Fig 7.2: The variation of S_n with β and ϕ' corresponding to k_h=0.1 and λ equals to: (a,c,e) 0 and (b,d,f) 1, with three different α's (kPa^{-1}): (a,b) α=0.1, (c,d) α=0.01 , and (e,f) α=0.001.

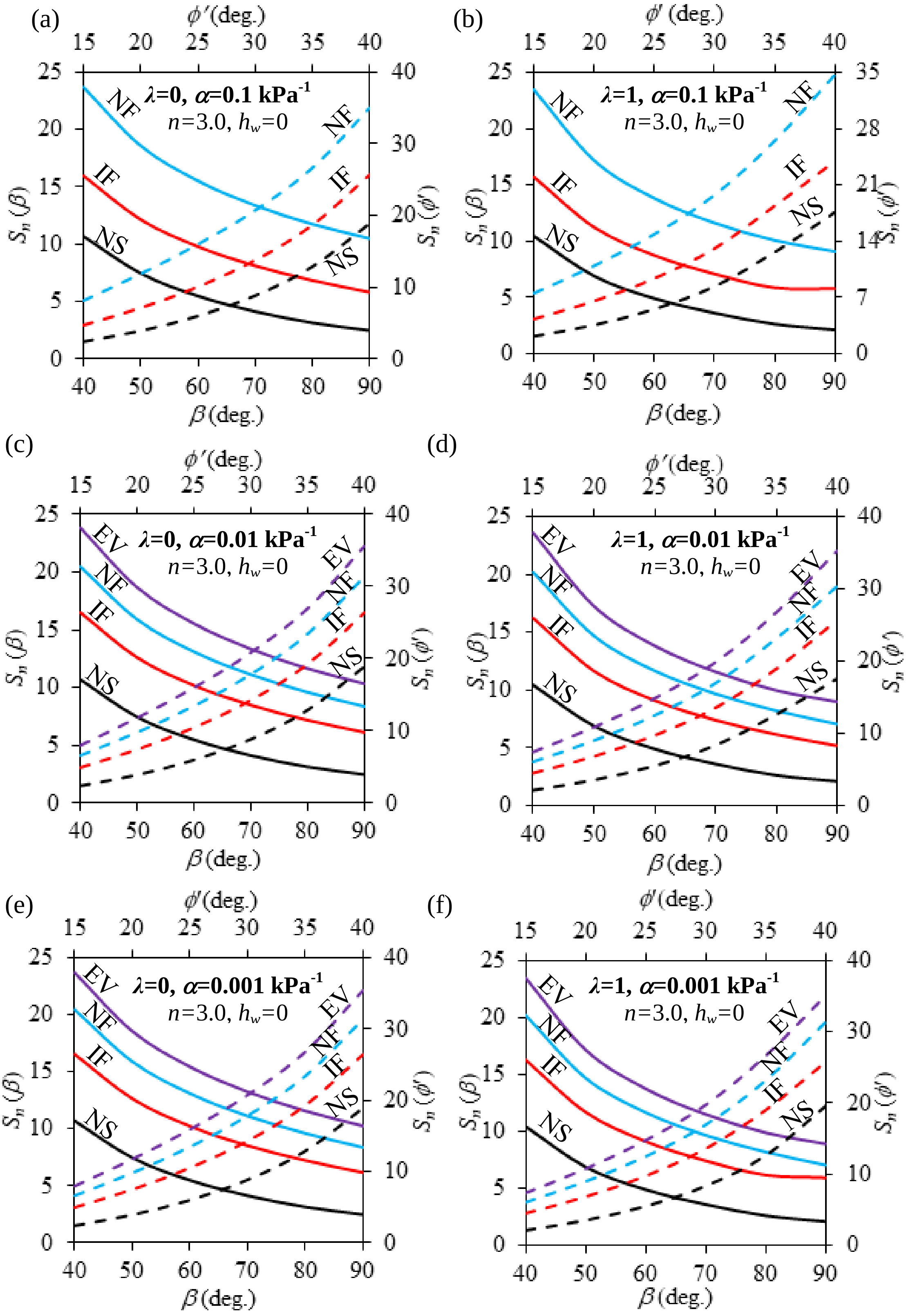

Note: (i) Solid and dashed lines represent S_n (β) and S_n (ϕ'), respectively.
(ii) EV: Evaporation; NF: No-Flow; IF: Infiltration; NS: No Suction

Fig 7.3: The variation of S_n and $S_n(\phi')$ curves corresponding to k_h=0.3 and λ equals to: (a,c,e) 0 and (b,d,f) 1, with three different α's (kPa^{-1}): (a,b) α=0.1, (c,d) α=0.01, and (e,f) α=0.001.

seem to be much impactful. This is further explored in Section 7.4.2. The steady-state flow direction impacts the $S_n(\beta)$ and $S_n(\phi')$ curves (refereed here as stability curves) in the similar manner. Regardless of the unsaturated properties and the seismic conditions, the evaporation-induced stability curves remain at the top and the stability curves pertaining to the no-suction state becomes the bottommost curves. Below the EV stability curve lies the NF stability curve and that is followed by IF stability curve. It can be interpreted that the evaporative condition yields the highest stability number, and the infiltrative flow results in the least stability number. The stability curves are plotted for various α values. The S_n values for upward water flow was coming to be complex number when α was considered to be 0.1; therefore, the EV stability curves, corresponding to α =0.1 were not attainable for both the considered k_h. Furthermore, the gap between the NF and IF stability curve shrinks for high AEV soils; the reduction of this gap seems to be quite appreciable when α decreases from 0.1 kPa^{-1} to 0.01kPa^{-1}, however, this gap is unnoticeable when α decreases from 0.01 kPa^{-1} to 0.001kPa^{-1}.

7.4.2 Impact of λ on S_n

Fig. 7.4 presents the variation of S_n with the parameter λ (referred here as $S_n(\lambda)$ curves) by varying the following parameters: (a) flow conditions (i.e. EV, IF, NF, NS), (b) k_h (=0.1 and 0.3) values, (c) n (=2 and 7) parameter, and (d) α (=0.1, 0.01, and 0.001 kPa^{-1}) parameter. The analysis is carried out for a constant ϕ' (=30°) and β (=45°). It is observed that the $S_n(\lambda)$ profiles remain almost horizontal indicating that the λ-value, or in other word the k_v value (for a constant k_h) has a negligible impact on the computed stability. Similar to the previous section, $S_n(\lambda)$ corresponding to EV is the topmost curve and it is subsequently followed by the NF, IF, and NS induced $S_n(\lambda)$ curves. The increase in k_h drastically reduces the stability value. The deviation of the

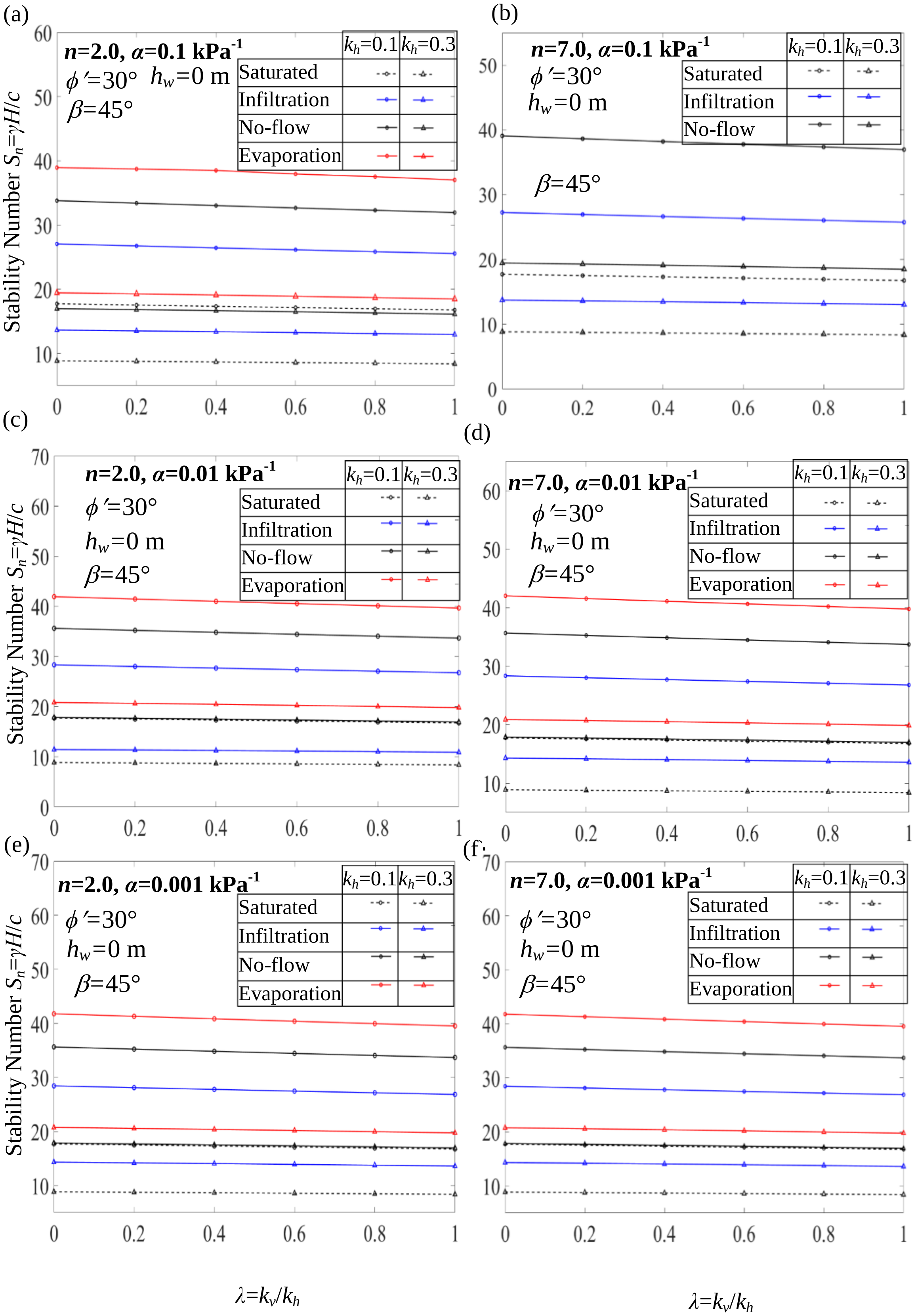

Fig. 7.4. The form of $S_n(\lambda)$ curves corresponding to various combinations of vG -model parameters: (a) n=2.0, α=0.1 kPa^{-1} , (b) n=7.0, α=0.1 kPa^{-1} , (c) n=2.0, α=0.01 kPa^{-1} , (d) n=7.0, α=0.01 kPa^{-1} , (c) n=2.0, α=0.001 kPa^{-1} , and (d) n=7.0, α=0.001 kPa^{-1}

$S_n(\lambda)$-profiles corresponding to k_h=0.1 and k_h =0.3 remains maximum for the EV flow and minimum for saturation state. There is a visible growth in the deviation between the $S_n(\lambda)$-curves when the soil is poorly-graded (n=7) in comparison to its well-graded (n=2) counterpart.

7.4.3 Impact of water table depth h_w on S_n

Fig. 7.5 depicts the variation of S_n with h_w (referred here as $S_n(h_w)$ curves) for a wide variety of soil types and water flows, conforming to various: (a) AEVs (α=0.1, 0.01, and 0.001 kPa^{-1}), (b) n (=2.0, 4.0, and 7.0) values, and (c) flow conditions (EV, NF, IF, and NS). The inclination (β=45°) and the frictional strength (ϕ=30°) of the soil are kept to be constant. Apparently, the $S_n(h_w)$ curves for the no-suction (i.e., saturation) condition remain to be the bottommost horizontal curves and unaffected by the α and n parameters. Irrespective of the vG-model parameters two distinct features are easily perceived: (a) $S_n(h_w)$ curve shows an nonlinear increasing trend, and (b) $S_n(h_w)$-NF curve always lies between $S_n(h_w)$-EV and $S_n(h_w)$-IF curves; an exception is being observed for α=0.1 kPa^{-1}, n=2.0 where the $S_n(h_w)$-EV curve displays an inverted 'V'-shape profile. For high α and n (e.g. α=0.1 kPa^{-1}, n=7.0), the $S_n(h_w)$-EV curve cannot be obtained, as the simulations were reporting imaginary values. As the AEV of the soil increases, there is a substantial improvement in the stability number. This improvement seems to be more pronounced when α varies from 0.1 kPa^{-1} to 0.01 kPa^{-1} rather than 0.1 kPa^{-1} to 0.01 kPa^{-1}. The influence of n becomes more visible for low AEV soils; the higher the n the higher the stability. Not only the stability magnitude, the vG model parameters also influence the trend of $S_n(h_w)$ curves. For relatively smaller α and n (e.g. α=0.1 kPa^{-1}, n=7.0), the $S_n(h_w)$ curves increase up to a certain GWT position and thereafter it manifests a horizontal plateau. This indicate the existence of a critical

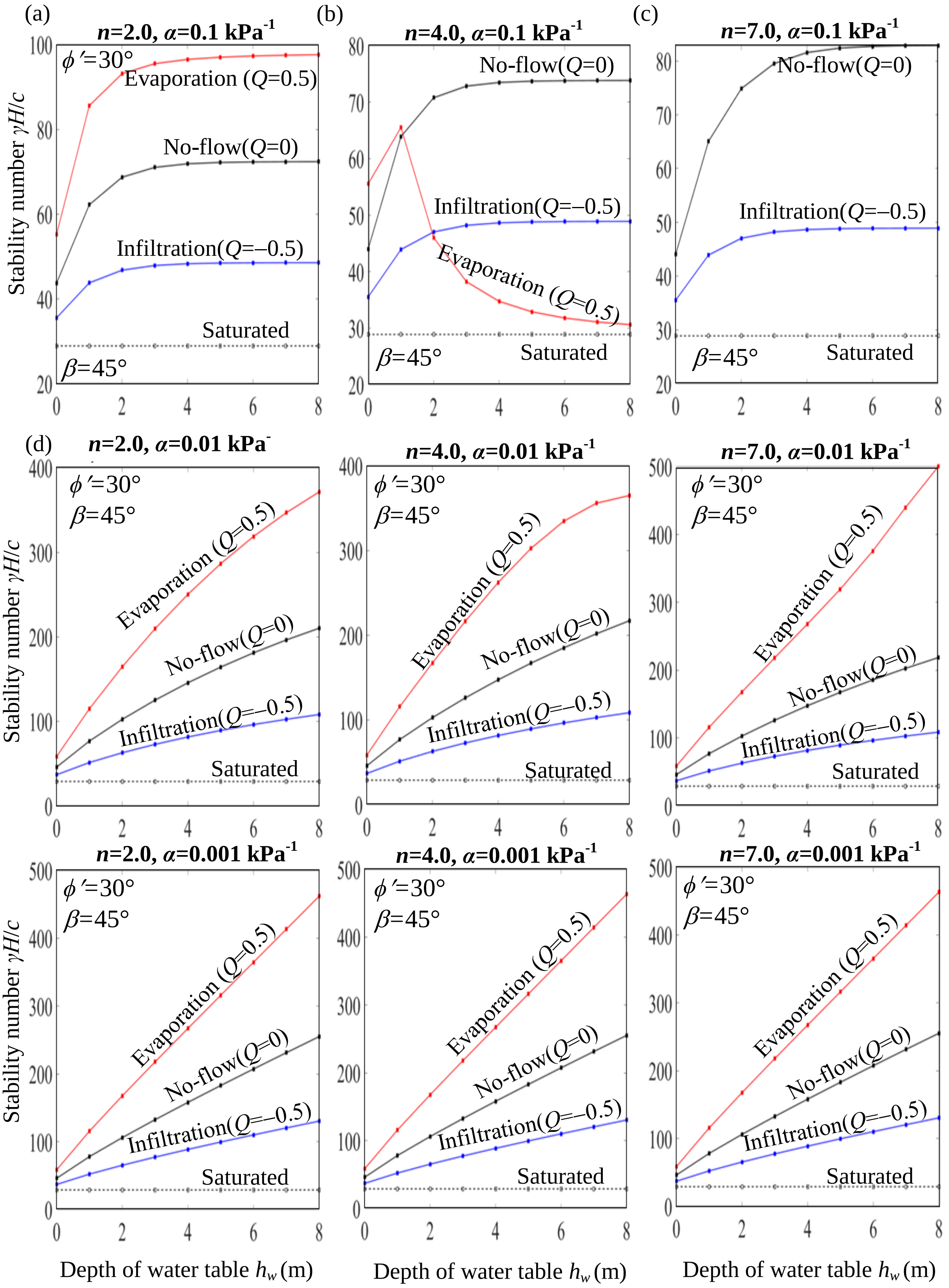

Fig. 7.5: The form of $S_n(h_w)$ curves corresponding to various combinations of vG *n*-parameter: (a, d, g) *n*=2.0, (b,e,h) *n*=4.0, (c,f,i) *n*=7.0 and vG *α*-parameter: (a,b,c) α =0.1 kPa^{-1} , (d,e,f) α =0.01 kPa^{-1} , and (g,h,i) α =0.001 kPa^{-1}

water table, especially for the coarse-grained soil, beyond which there is no further improvement of the stability. With the increase in α, the $S_n(h_w)$ curves exhibit a continuous increasing trend. The n-value also reduce the curvature of the $S_n(h_w)$ curves.

7.4.4 Combined impact of k_h and h_w *on* S_n

Fig. 7.6 depicts the combined effect of horizontal seismic coefficient (k_h) and GWT depth (h_w) on stability number (S_n) for various α and λ. The three-dimensional curves are plotted for 45° slope without the application of any surcharge pressure. The soil is having a frictional strength of 30° and is subjected to relatively high infiltration ($Q= -0.8$). These three-dimensional surfaces, in a sense, represent the combined effect of the seismic loading and the GWT position that are discussed in the previous sections. The profile seems to be nonlinear wrapped one. Apparently, S_n increases with the lowering of the GWT. This improvement in the stability happens to be more visible for the static loading rather than the pseudo-static one. The combined influence of soil's air-entry value, GWT position, and the horizontal and vertical seismic forces are clearly discernible from the obtained three-dimensional surfaces.

7.4.5 Impact of surcharge load (p_s)on S_n

Fig. 7.7 depicts the variation of S_n with p_s (referred here as $S_n(p_s)$ curves) for a wide variety of vG parameters conforming to two different friction angles, namely $\phi'=20°$ and $\phi'=35°$. The simulations were carried out by considering $\beta = 50°$, $h_w=2$m, $Q = -0.3$. For the verification of n parameter on $S_n(p_s)$ curves, α is taken to be 0.05 kPa^{-1}, whereas for investigating the impact of α parameter on $S_n(p_s)$ curves, the magnitude of n is adopted as 6. No matter whatsoever be the unsaturated properties, $S_n(p_s)$ curves always show a decreasing trend. For $\phi'=20°$, the n parameter hardly impacts the $S_n(p_s)$ curves. Nevertheless, the soils with relatively higher strength ($\phi'=35°$) exhibit notice-

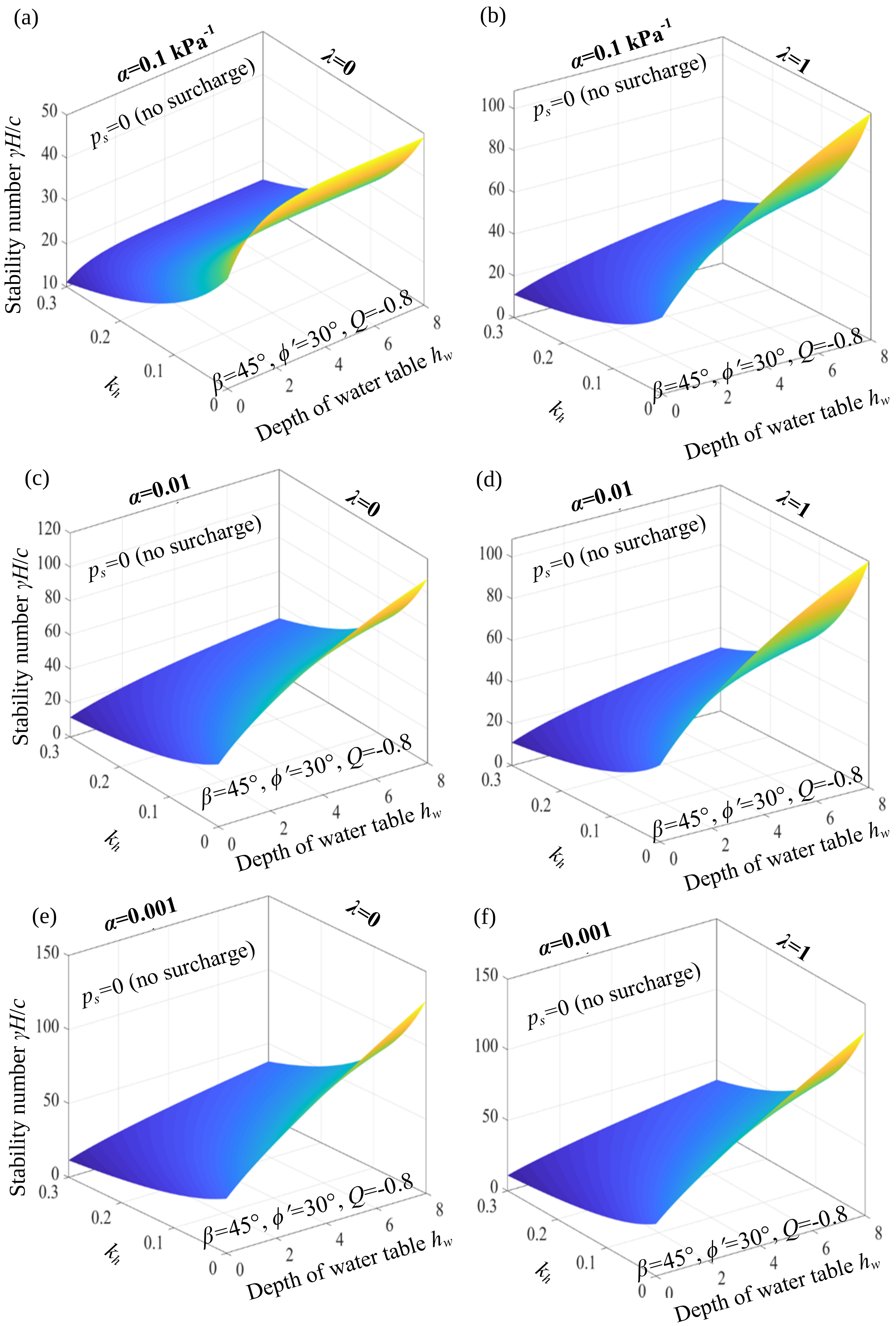

Fig. 7.6 The three-dimensional stability profiles in $S_n - k_h - h_w$ space for three different α's: (a,b) α =0.1 kPa^{-1}, (c,d) α =0.01 kPa^{-1}, and (e,f) α =0.001 kPa^{-1} and two λ's (a,c,e) λ=0 and (b,d,f) λ=1.

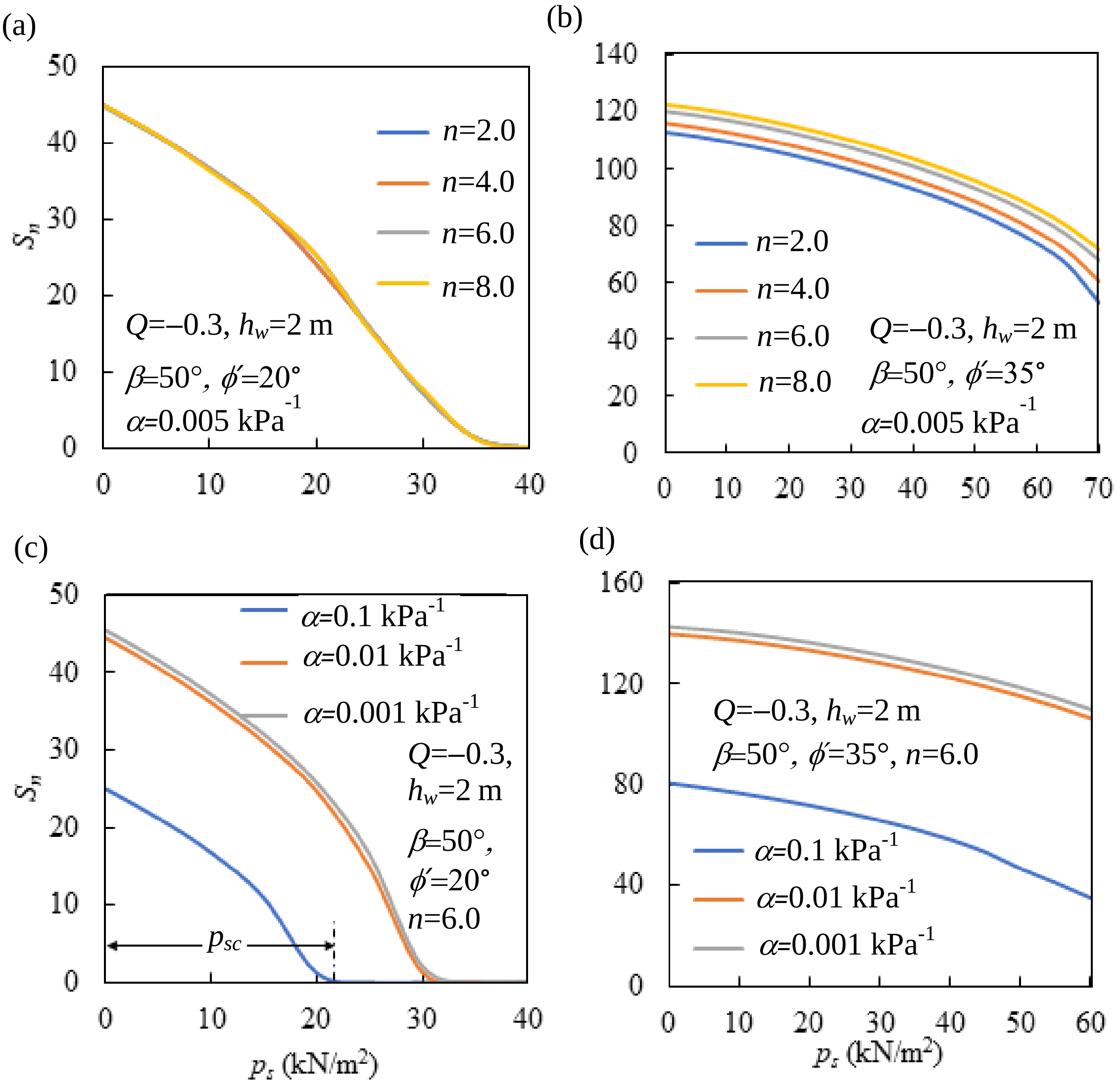

Fig. 7.7: Variation of S_n with surcharge load p_s with respect to (a) and (b) vG parameter n; (c) and (d) vG parameter α.

able influence on the $S_n(p_s)$ curves; the $S_n(p_s)$ curve pertains to lower n remains in the bottom side. Conversely, the vG-α parameter plays a dominating role in dictating the form of the $S_n(p_s)$ curves. The changes in $S_n(p_s)$ profiles are highly observable when α changes from 0.01 kPa^{-1} to 0.1 kPa^{-1}; the higher the α lower the stability values. The decreasing trends of the $S_n(p_s)$ curves clearly reveal the presence of certain p_s at which S_n will attain zero magnitude; this certain p_s is designated here with the symbol p_{sc}. The magnitude of p_{sc} becomes very less for a weaker soil with very low AEV. For a stronger soil (e.g. $\phi'=35^{\circ}$) the attainment of p_{sc} happens to be at a very large surcharge pressure, because the decrement rate of $S_n(p_s)$ curves occurs at a relatively slow pace.

Fig. 7.8 depicts the three-dimensional form of the stability chart by combining the effect of p_s and air entry value on the computed S_n. The other input parameters are chosen as: $\beta=45°$, $\phi'=25°$, $Q=-0.4$. Figs. 7.8a and 7.8b correspond to $h_w=4$ m and $h_w=0$m, respectively. It is inferred that, with increasing h_w, the slope can withstand more load (surcharge), and correspondingly, the magnitude of p_{sc} enhances.

7.5 FAILURE SURFACES

Fig. 7.9 presents a comparative study of the failure surfaces generated for a representative slope with slope angle $\beta=45°$ and water table lying at the toe ($h_w=0$). Only the hydrostatic condition is considered. It is inferred from the plots that, for both $\lambda=0$ and $\lambda=1$, the log spiral surface shifts to the right (this means more soil is captured inside the log spiral failure zone), as the value of k_h increases from $k_h=0.0$ to $k_h=0.3$. Moreover, the spread of log spiral is more pronounced for $\lambda=0$ than $\lambda=1$.

7.6 COMPARISON WITH LITERATURE

To verify the efficacy and the accuracy of the proposed methodology, the failure surfaces obtained from the present analysis are compared with that of Vahedifard et al. (2016) for a representative slope with parameters: $\beta=70°$, $\phi=25°$, and non-seismic, surcharge-less conditions, as presented in Fig. 7.10. Two characteristic cases are used for the comparative study: no suction condition (NS), and unsaturated soil with $\alpha=0.005$ kPa^{-1}, $n=2.0$, no flow ($Q=0$). It is observed that the failure surfaces obtained from the present computational method match quite well with those by Vahedifard et al. (2016). It is noteworthy that the NS failure envelopes generated by the two studies

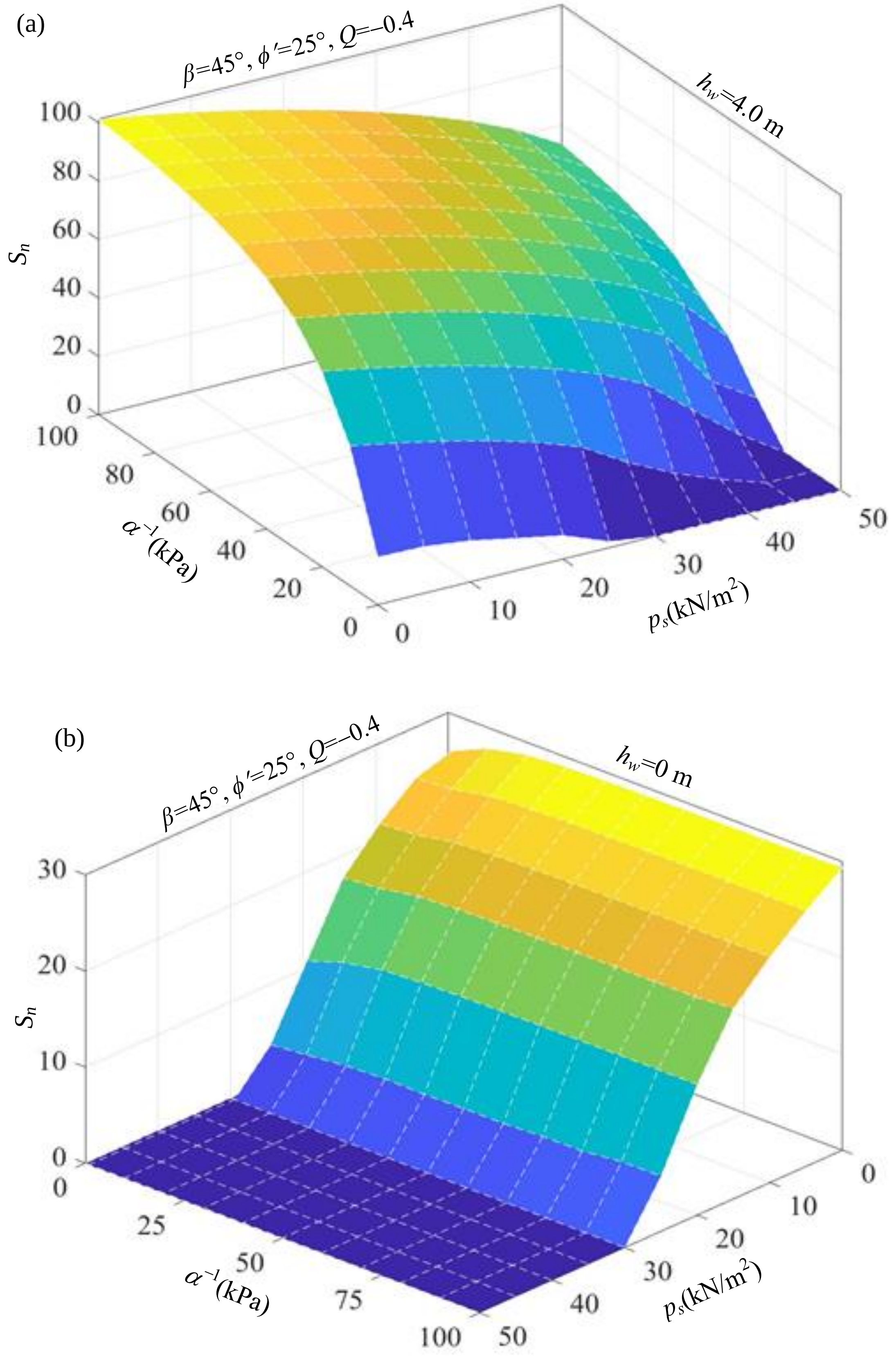

Fig. 7.8: Three dimentional represention of the variation of S_n with vG parameter α and p_s conforming to the parameters: ϕ'=25°, Q=–0.4, β=45° for (a) h_w = 4.0 m and (b) h_w = 0 m.

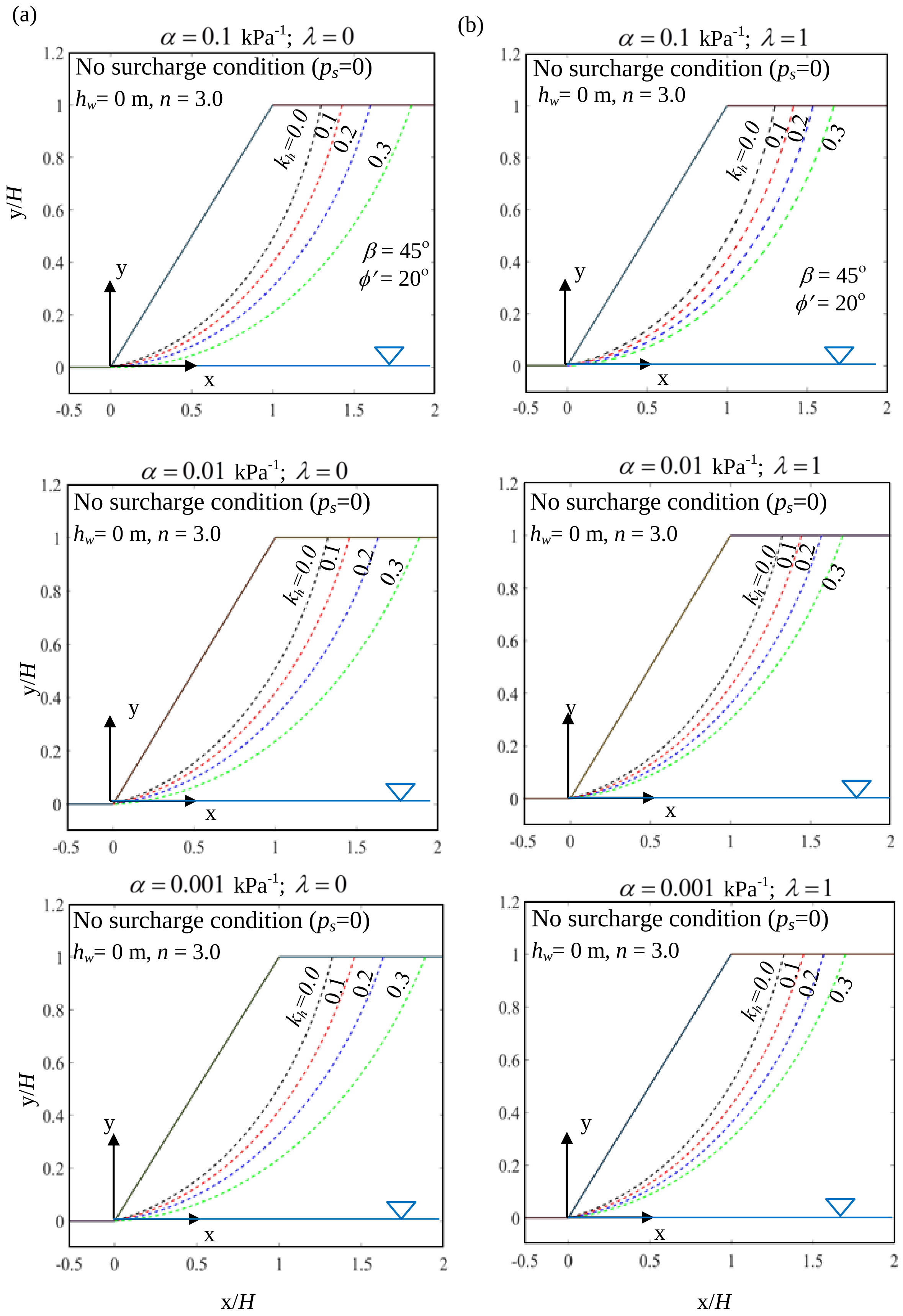

Fig. 7.9 The form of the developed failure surfaces corresponding to $\beta = 45^{\circ}$, $\phi' = 20^{\circ}$, $h_w = 0$ m, $n = 3.0$ and conforming to (a) α=0.1 kPa^{-1}; λ=0 , (b) α=0.1 kPa^{-1}; λ=1, (c) α=0.01 kPa^{-1}; λ=0, (d) α=0.01 kPa^{-1}; λ=1, (e) α=0.001 kPa^{-1}; λ=0, (f) α=0.001 kPa^{-1}; λ=1.

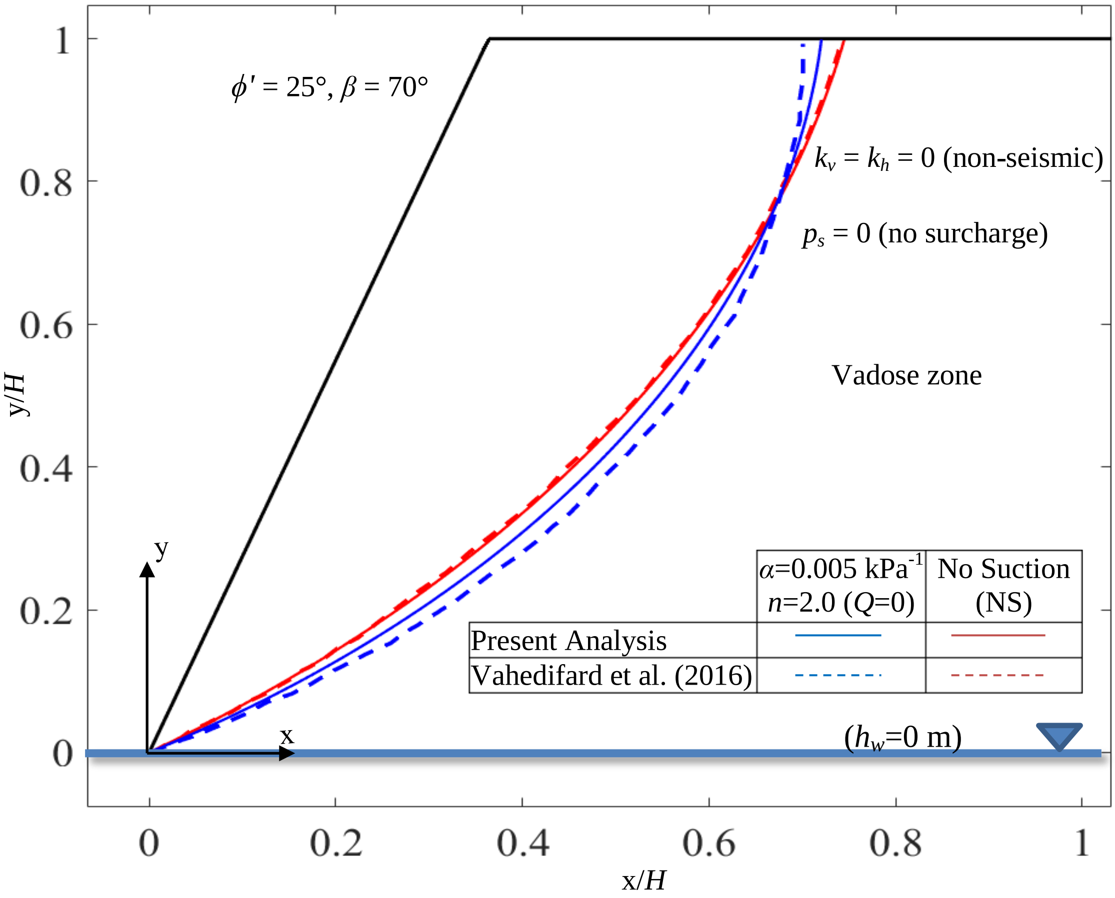

Fig. 7.10: Log-spiral failure surfaces generated for two soil types, namely, an unsaturated soil (α=0.005 kPa^{-1}, n=2.0) and a saturated soil (no suction) for the representative slope with geometric parameters: β=70°, ϕ'=25°. The surfaces generated with the present analysis are compared with that of Vahedifard et al. (2016).

almost exactly match each other. Fig. 7.11 depicts a comparative study of two vertical slopes (β=90°) with characteristics: α=0.005 kPa^{-1}, n=2.0, no flow (Fig. 7.11a); α=0.1 kPa^{-1}, n=5.0, no flow (Fig. 7.11b) for non-seismic, surcharge-less conditions. Taylor's stability number (TSN) is varied with internal friction angle ϕ'. Taylor's stability number (N_s) is defined as $c_d/\gamma H$, where $c_d=c/F_s$, which is nothing but the algebraic reciprocate of Chen's stability number S_n. It is observed that the NS envelopes of all three studies (present analysis, Sun et al. 2019, Vahedifard et al. 2016) approximately coincide. However, for the unsaturated conditions (for both soil types

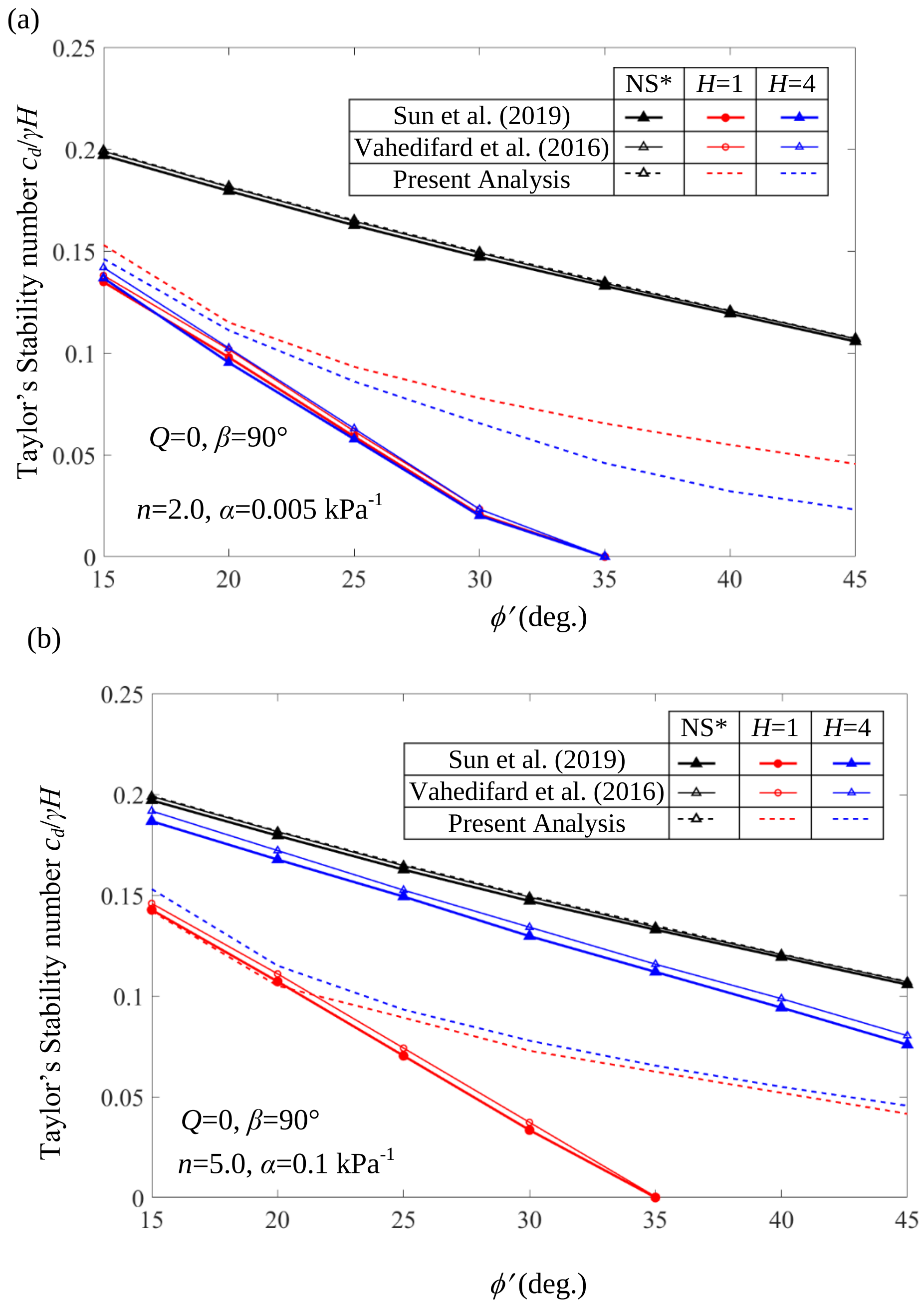

Note: *NS= No Suction

Fig. 7.11 A comparison of stability number obtained from present study with the solution of Sun et al. (2019) and Vehedifard et al. (2016) considering (a) α=0.005 kPa^{-1} and (b) α=0.1 kPa^{-1}.

and heights H = 1 m and H = 4 m) the present solution yields the highest TSN compared to the literature, hence predicting more conservative results coupled with its upper bound nature. Results from Zhao et al. (2016) were used to validate the output of the pseudo-static response of the present analysis. Fig. 7.12 presents the comparative variation of S_n with the parameter λ ($\lambda = k_v/k_h$) for three characteristic k_h values, viz., k_h=0.1, k_h=0.2, and k_h=0.3. The slope is saturated and has the following geometric and strength parameters: β=45°, ϕ'=20°. The trend observed from the present analysis matches quite exactly with Zhao et al. (2016); in fact, the present analysis methodology yields lesser S_n values than Zhao et al. (2016), hence providing better upper bound solutions.

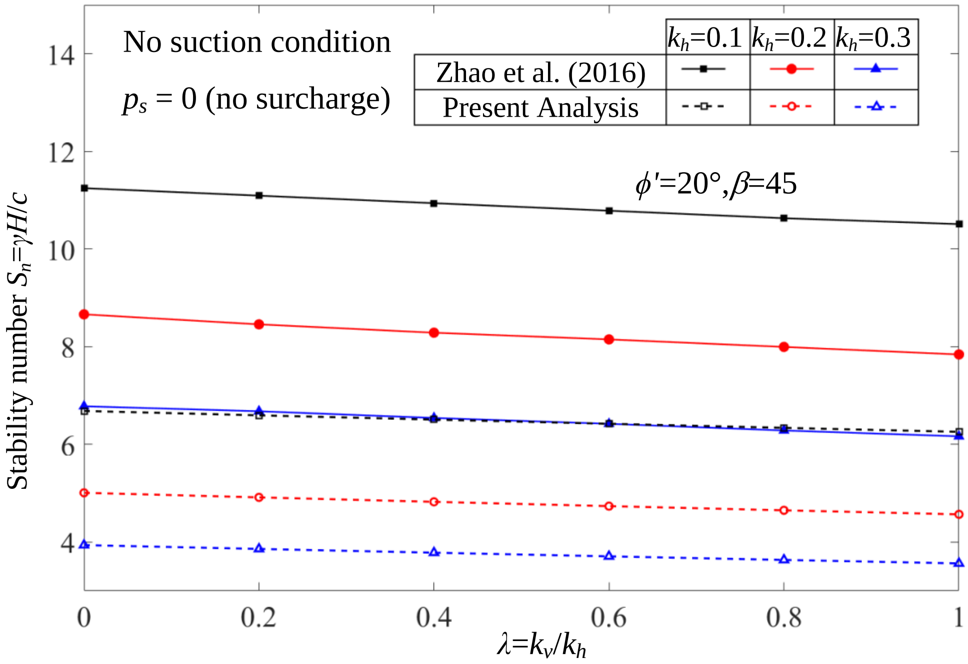

Fig. 7.12 A comparison of stability number obtained from present study and the solution of Zhao et al. (2016) for different k_h.

7.7 SUMMARY

This chapter focuses on the computation of the stability number (S_n) for homogeneous unsaturated slopes under seismic and surcharge loads. The effect of various factors such as water table depth, adverse climatic conditions, and varying slope geometry, are extensively verified. The unified suction-stress-based effective stress formulation is employed to simulate the problem, providing a comprehensive understanding of stability analysis. Parametric analysis is conducted by varying soil properties, allowing for a thorough exploration of the combined effects of water table depth and seismic forces on slope stability. The study also investigated the impact of water table depth and surcharge load on slope stability, visualizing the results in 3D charts. The computed solutions are validated through a comparison with available literature, showing good agreement and reinforcing the reliability of the proposed methodology. Failure surfaces are plotted for different soil strength parameters and loading conditions, offering valuable insights into slope behaviour. The use of an implicit optimization technique improves the computation accuracy and efficiency, representing a significant advancement. The proposed stability charts provide guidance to engineers, enabling the assessment of slope stability in homogeneous unsaturated soil under seismic and surcharge loading conditions.

7.8 LIMITATIONS

The present study makes certain assumptions for simplicity, assuming homogeneous soil properties throughout the slope, which may oversimplify real-world conditions and potentially lead to conservative results. The study overlooks spatial variations in soil properties, ignores the impact of dilation angle and stiffness parameters, and assumes that the water table never intersects the failure mechanism. Climatic variations, such as wetting fronts during heavy rainfall, are not considered, limiting the study’s coverage of possible influences on slope stability. While parametric analysis is conducted by varying soil properties, the range of variations may not encompass all potential soil conditions. The findings are confined to the selected parametric variations. When the required field parameters exceed the defined ranges, determining the stability number can be seamlessly accomplished through the provided formulas.